The impact of optimal selected historical forecasting samples on hybrid ensemble-variational data assimilation

Yaodeng Chen[a,*], Shan Guo[a], Deming Meng[a], Hongli Wang[b,c], Dongmei Xu[a], Yuanbing Wang[a], Jia Wang[a]

[a] *Key Laboratory of Meteorological Disaster of Ministry of Education (KLME) / Joint International Research Laboratory of Climate and Environment Change (ILCEC) / Collaborative Innovation Center on Forecast and Evaluation of Meteorological Disasters, Nanjing University of Information Science & Technology, Nanjing 210044, China*
[b] *Cooperative Institute for Research in Environmental Sciences, University of Colorado, Boulder, United States*
[c] *NOAA/OAR/Earth System Research Laboratory/Global Systems Division, Boulder, CO, United States*

ABSTRACT

A resampling method that selects historical forecasting samples as supplementary samples is proposed for the hybrid ensemble-variational data assimilation system to alleviate the computational burden of ensemble forecasting samples. To select reasonable samples from all historical forecasting samples, the first modes of absolute vorticity are abstracted by the empirical orthogonal function (EOF) as indicators of atmospheric dynamic features from the background and each of historical forecasting sample, then they are matched at the analysis time. A series of single observation tests and 19-day cycling data assimilation and forecasting experiments for a Mei-yu period are carried out to evaluate the impact of the selected historical forecasting samples.

The single observation tests indicate that the use of selected historical forecasting samples is able to provide reasonable flow-dependent background error covariance for the data assimilation system. The cycling data assimilation and forecasting experiments demonstrate that the analyses and forecasts as well as precipitation forecast skills are improved by using the combination of selected historical forecasting samples and ensemble forecasting samples. The sample-combined experiment performs close to the experiment with full-size ensemble forecasting samples, but it spends fewer computational resources. The diagnosis of a heavy rainfall case is presented to further illustrate the role of the selected historical forecasting samples. It is found that the simulation of vertical velocity and relative humidity are improved for the case in the experiment of the combined samples, leading to better intensity and position forecasts of the precipitation.

1. Introduction

With the increasing of meteorological observation data, data assimilation methods have been widely used as an effective way to improve the initial conditions for advancing the forecast skill of numerical weather prediction. Three-dimension variational (3DVar; Lorenc, 1986) is commonly applied in various assimilation systems because of its simplicity, but its background error covariance is usually isotropic and homogeneous (Xue et al., 2003). Four-dimension variational (4DVar; Dimet and Talagrand, 1986) allow the evolution of the background error covariance, but the development and maintenance of the adjoint and tangent linear models are quite complicated (Huang et al., 2009). The flow-dependent background error covariance can be derived from the ensemble Kalman filter (EnKF; Evensen, 1994) method. Nonetheless, EnKF is hampered by rank deficiency, unbalance between variables in analysis, and sampling errors with limited sample size (Evensen, 2003).

The hybrid method that incorporates the ensemble-based approach within the variational assimilation system as an alternative assimilation technique firstly proposed by Hamill and Snyder (2000). Due to its great potential, it has been one of the research focuses of assimilation (Lorenc, 2003; Wang et al., 2008a, 2008b; Zhang et al., 2013; Schwartz and Liu, 2014; Lorenc et al., 2015; Bannister, 2017). This method takes advantage of the strength of EnKF and variational methods, and alleviates the rank deficiency problem of EnKF caused by sample insufficiency as well as provides flow-dependent covariance instead of static, homogeneous and isotropic background error covariance in 3DVar. However, the rationality of flow-dependent background error covariance derived from the hybrid method largely depends on the sufficient ensemble samples, which requires plenty of computing

* Corresponding author.
  E-mail address: keyu@nuist.edu.cn (Y. Chen).

resources.

In order to cut down the computational costs required by the ensemble samples and introduce the inhomogeneous and anisotropic background error covariance at the same time, some efforts have been devoted to this research field recently. For instance, the time-lagged ensemble method was employed in hybrid data assimilation system to improve the structure of wind (Wang et al., 2017). The historical forecasting samples calculated in the past are also utilized to take the place of ensemble forecasts in hybrid data assimilation system. The method based on historical forecasting samples costs as much as 3DVar, but performs better in analysis and forecasts than 3DVar due to the introduction of inhomogeneous background error covariance (Chen et al., 2018). However, the background error covariance estimated from all unselected historical forecasting samples is liable to embody clearly climatic features of the past period rather than reflect the present weather condition well.

Nevertheless, it is likely that some of the historical forecasting samples may represent the current weather situation at the moment of assimilation (Van den Dool, 1989, 1990). In order to use historical forecasting samples in a reasonable way, empirical orthogonal functions (EOF) are employed as a tool for dimensionality reduction (Monahan et al., 2009) to extract the spatial patterns as meteorological features from three-dimensional variable fields of samples and background. Then the spatial patterns from historical samples and background are matched at the time of assimilation to select the samples which are closer to the synoptic situation of the background. After that, the selected historical forecasting samples are introduced to combine with small-size ensemble forecasting samples so as to avoid the computation of full-size ensemble forecasting samples. The combination of selected historical forecasting samples and ensemble forecasting samples meets the requirements of introducing flow-dependent features and reducing computational costs.

The structure of this study is organized as follows, in Section 2, the methodology of hybrid including the usage of historical forecasting samples is described. The selection process of historical forecasting samples by EOFs is explained in detail in Section 3. The single observation data assimilation experiments are discussed in Section 4. The cycling data assimilation and forecasting experimental design and evaluation of results are presented in Section 5. The diagnostic results for a heavy rainfall case are shown in Section 6. A summary and conclusion are given in the final Section 7.

2. Methodology

The cost function of hybrid method is defined as follows (Wang et al., 2008a, 2008b):

$$J(\delta \mathbf{x_1}, \boldsymbol{\alpha}) = \beta_1 \frac{1}{2} \delta \mathbf{x_1}^T \mathbf{B}^{-1} \delta \mathbf{x_1} + \beta_2 \frac{1}{2} \boldsymbol{\alpha}^T \mathbf{A}^{-1} \boldsymbol{\alpha} + \frac{1}{2} (\mathbf{d} - \mathbf{H} \delta \mathbf{x})^T \mathbf{R}^{-1} (\mathbf{d} - \mathbf{H} \delta \mathbf{x}) \tag{1}$$

The first term of Eq. (1) represents the traditional variational assimilation background term with static background error covariance (**B**). The second term represents the background term associated with flow-dependent background error covariance derived from the ensemble differences. The vector $\boldsymbol{\alpha}$ is ensemble extended control variable and **A** defines the spatial covariance of $\boldsymbol{\alpha}$. Factors β_1 and β_2 are the weights for the static homogeneous covariance and inhomogeneous covariance respectively, and both of them are constrained by $1/\beta_1 + 1/\beta_2 = 1$. The third term of the right hand is the observation term, of which **R** is the observation error covariance, **d** is the innovation vector, and **H** denotes the linearized observation operator. $\delta \mathbf{x}$ is the analysis increment of the hybrid method, defined as,

$$\delta \mathbf{x} = \delta \mathbf{x_1} + \sum_{k=1}^{N} (\boldsymbol{\alpha}_k \circ \mathbf{x}_k^e) \tag{2}$$

where $\delta \mathbf{x_1}$ is the increment associated with the static background covariance. The second term represents a local linear combination of ensemble differences associated with the inhomogeneous ensemble covariance. $\boldsymbol{\alpha}$ used in Eq. (1) is a vector formed by concatenating vectors $\boldsymbol{\alpha}_k$ ($k = 1, …, N$). N is the total number of the ensemble members and the symbol $\circ$ denotes the product element by element of vectors $\boldsymbol{\alpha}_k$ and $\mathbf{x}_k^e$.

In order to reduce the computational burden of ensemble forecasts as well as retaining the equal full sample size, selected historical forecasting samples are introduced to combine with a portion of ensemble forecasting samples. Therefore, there are two sources of ensemble differences $\mathbf{x}_k^e$. One is the real ensemble differences $\mathbf{x}_{Ek}^e$, and the other is the historical ensemble differences $\mathbf{x}_{Hk}^e$. $\mathbf{x}_{Ek}^e$ is normalized by $\sqrt{N_E - 1}$ and $\mathbf{x}_{Hk}^e$ is normalized by $\sqrt{N_H - 1}$ as follows:

$$\mathbf{x}_{Ek}^e = (\mathbf{x}_{Ek} - \overline{\mathbf{x}_E}) / \sqrt{N_E - 1} \tag{3}$$

$$\mathbf{x}_{Hk}^e = (\mathbf{x}_{Hk}^{diff} - \overline{\mathbf{x}_H}) / \sqrt{N_H - 1} \tag{4}$$

$$\mathbf{x}_{Hk}^{diff} = \mathbf{x}_{Hk}^{T_1} - \mathbf{x}_{Hk}^{T_2} \tag{5}$$

In Eq. (3), $\mathbf{x}_{Ek}$ ($k = 1, …, N_E$) is the k_{th} ensemble member, $\overline{\mathbf{x}_E}$ is the ensemble mean and N_E is the number of ensemble differences. In Eq. (5), $\mathbf{x}_{Hk}^{diff}$ ($k = 1, …, N_H$) is defined as the ensemble differences. T_1 and T_2 are forecast leading times. In Eq. (4), $\overline{\mathbf{x}_H}$ is the mean value of all the historical ensemble differences, and N_H is the number of historical ensemble differences. $\mathbf{x}_{Hk}^e$ is the historical ensemble differences calculated from the selected historical forecasting samples. The concrete selection method is presented in Section 3.

3. Selection of history forecasting samples

3.1. Selection process

The empirical orthogonal functions (EOF; Wallace and Gutzler, 1981) method is utilized to select the historical samples that are more consistent with the current weather conditions at the analysis time, in order to obtain more reasonable forecast error mentioned in Section 2. The synoptic-scale weather characteristics can be extracted from all historical forecasting samples and background, and then better historical forecasting samples will be picked referring to the matching degree between the features of background and historical forecasting samples. As for the indicator, the absolute vorticity is regarded as a referential variable since it represents the rotation of airflow and plays an important role in other advanced diagnostic quantities of weather system (Prezerakos et al., 1997; Ran et al., 2013). There are four specific procedures for the selection process:

1) At the initial moment of assimilation, the absolute vorticity of all historical forecasting samples and current-time background are calculated and then decomposed in the vertical direction by applying the EOF method. Therefore, the space patterns of the absolute vorticity extracted from historical samples and background after dimensionality reduction are obtained and used for selection.
2) In order to utilize the space patterns of historical samples and background, the correlations between the first modes of the absolute vorticity derived from each historical forecasting sample and current-time background are then calculated.
3) Ranking the historical forecasting samples in descending order according to the correlations.
4) The historical forecasting samples are selected according to the ranking order and then introduced in the hybrid data assimilation scheme. For example, in this study the top 30 historical forecasting samples are used in the sample-combined hybrid experiment and the remaining lower ranking historical samples are discarded.
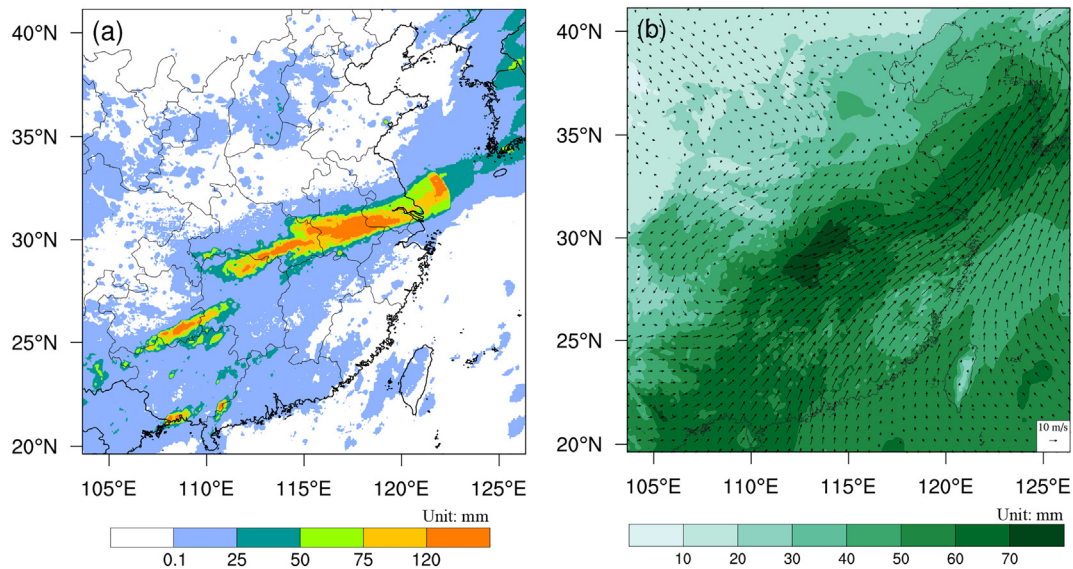
Fig. 1. (a) The distribution of 24 h accumulated precipitation initialized at 0600 UTC 01 July 2016 (shaded; mm) from the China Hourly Merged Precipitation Analysis (CHMPA), (b) the horizontal wind (vector; m s^{-1}) at 850 hPa and the precipitable water (shaded; mm) derived from Global Forecast System (GFS) analysis valid at 0600 UTC 01 July 2016.

3.2. Features of the historical forecasting samples

National Meteorological Center (NMC; Parrish and Derber, 1992) method is applied to calculate the original historical forecasting samples which are the difference between 24 h and 12 h forecasts valid at the same time (i.e., every 0000, 0600, 1200 and 1800 UTC). As a result, the original 139 pairs of historical forecasting samples are obtained covering a typical Mei-yu period from 0000 UTC 7 June to 1800 UTC 12 July 2015.

3.2.1. Atmospheric feature of the background

To further discuss the selection method in detail, an instance of the selection process is analyzed. The 24 h accumulated precipitation from 0600 UTC 01 July 2016 to 0600 UTC 02 July 2016 reported by China Hourly Merged Precipitation Analysis (CHMPA; Shen et al., 2014) is displayed in Fig. 1a. As is shown in Fig. 1a, the rain belt lay from southwest to northeast in the Jianghuai area of eastern China. In this rainfall process, the accumulated precipitation over the Jianghuai area reached 584.3 mm and ranked 3th largest since 1951. The anomalously high precipitation leads to serious flood disasters (Yuan et al., 2017). The 850 hPa horizontal winds and precipitable water derived from the Global Forecast System (GFS) analysis are shown in Fig. 1b. It can be seen that there is a shear line along the rain belt. Warm and moist air is carried to the Jianghuai area by southwest flow from Bengal Bay. As a consequence, the heavy precipitation process in the Jianghuai area occurred due to the cooperation of the gathered water vapor and the strong ascending motion of the Jianghuai cyclone.

Fig. 2 shows the distribution of absolute vorticity and atmospheric circulation of the background derived from the Global Forecast System (GFS) analysis valid at 0600 UTC 01 July 2016. It can be seen that the distribution of vorticity and atmospheric circulation has a similar pattern (Fig. 2). At 850 hPa, the positive vorticity is distributed along the wind shear line near 30°N in east China (Fig. 2a), where the Mei-yu front develops and causes heavy rains (Chen and Tai-Jen, 2004). At 500 hPa, there exists a low-pressure trough in eastern China. In addition, it shows that northward motion and extension of the West Pacific subtropical anticyclone (Fig. 2b), which is also important for Mei-yu precipitation (Gao et al., 2002). At 200 hPa, the anticyclone is dominant in the Jianghuai area, which indicates the eastward-moving of South Asia high. The absolute vorticity is relatively smaller at 500 hPa than 850 hPa (Fig. 2c). This configuration of atmospheric flow and

vorticity lead to intensive convection activity, which causes the convergence of moisture and continuous heavy rainfall (Sampe and Xie, 2010). Also, its relatively regular atmospheric pattern during the typical Mei-yu period makes it possible to introduce the historical forecasting samples with similar atmospheric circulation as part of ensemble samples in the assimilation system.

Although convection strongly depends on the low-level dynamic factors, it is not solid to elucidate the cause of the Mei-yu system (Sampe and Xie, 2010). It means that the influences over the rainfall process are noticeable from both low-level and upper absolute vorticity. To comprehensively consider the influence of absolute vorticity at different heights, the EOF method is used to compress the three-dimensional variables in the vertical direction into the two-dimensional spatial patterns with meteorological features. Thus, the background information of the absolute vorticity on different levels is orthogonally decomposed and extracted in EOF spatial patterns. The spatial patterns of the first three leading modes are showed in Fig. 3. In the first leading mode (Fig. 3a), the pattern between the negative absolute vorticity and the main rainfall area is more similar than that of the other two modes (Fig. 3b-c).

More variances such as the potential vorticity (hereafter "PV") and temperature in the background are abstracted by the EOF method to be tested. Fig. 4 shows the horizontal distribution of the PV in 850 hPa, 500 hPa and 200 hPa and the spatial patterns of the first three leading modes of the decomposed PV and temperature at 0600 UTC 1 July 2016. It can be seen that the distribution of PV (Fig. 4a-c) has significant differences from that of the absolute vorticity (Fig. 2) in different levels. The different results of PV could be explained by the perspective of formulas. In z coordinate system, the PV is defined as $\frac{\xi_a \cdot \nabla \theta}{\rho}$ where ξ_a is the absolute vorticity, ρ is density, and ∇θ is the gradient of potential temperature. It means that PV is a variable that combines the dynamic factor and thermodynamic factor. The results show that both factors are significant at individual levels. However, in the EOF space, the spatial patterns of PV (Fig. 4d-f) are completely different from absolute vorticity (Fig. 3). More horizontally uniform features can be seen (Fig. 4d) and the contribution rate of the first mode of PV reaches to 96.7% far more than absolute vorticity's (32.5%, Fig. 3a). This is because the PV in EOF space is dominated by a large vertical variation which is horizontally uniform. While it might be beneficial to try subtracting a horizontally uniform PV distribution before transforming to EOFs, for the present work the first mode of the
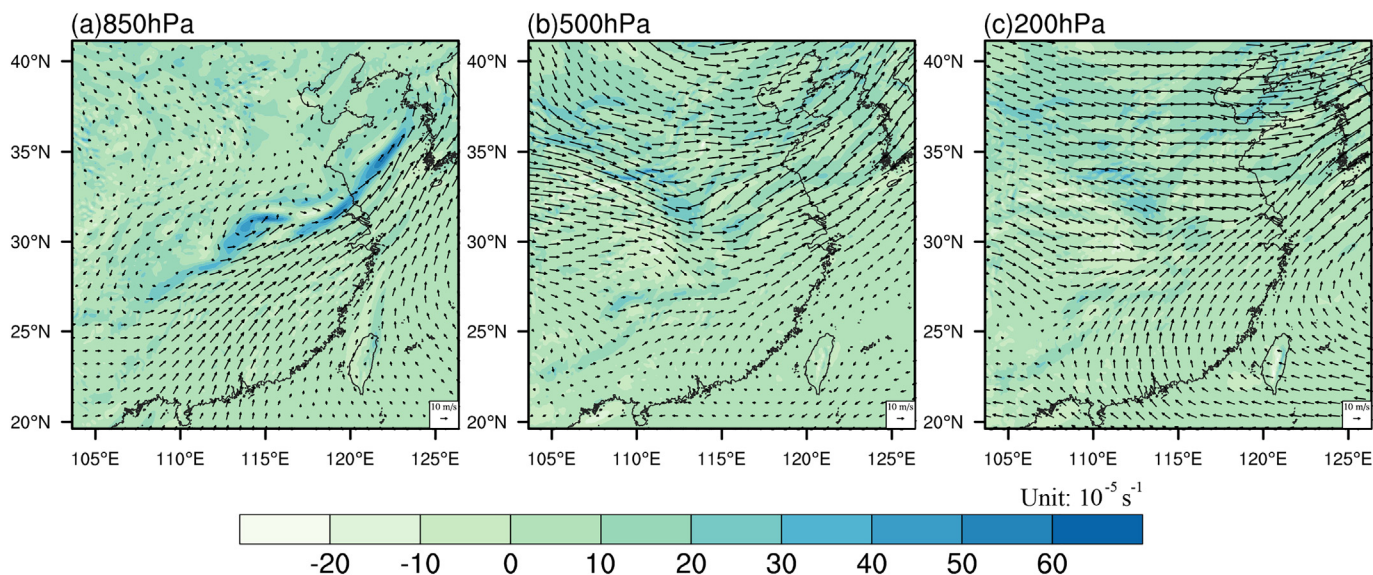
Fig. 2. The horizontal distribution of atmospheric circulation (vector; m s^{-1}) and absolute vorticity (shaded; 10^{-5} s^{-1}) at (a) 850 hPa, (b) 500 hPa, (c) 200 hPa derived from GFS analysis at 0600 UTC 1 July 2016.

absolute vorticity from the background is used as a reference standard for selection in subsequent research.

3.2.2. Analysis of the selection results

The rankings of the first modes in the 139 historical forecasting samples are displayed in Fig. 5. They are arranged according to the correlations calculated with background valid at 0600 UTC 1 July 2016. The first modes with the highest and lowest correlation coefficients are shown in Fig. 5a and Fig. 5o respectively, and others are displayed at an interval of ten rankings (Fig. 5b-n). It can be seen that the first modes of historical forecasting samples sorted in the first 30th are closer to the first mode of background (Fig. 5a-d). Basically, a strip-shaped negative area in the Mei-yu area can be seen in the first 50th ranking (Fig. 5a-f). For the historical forecasting samples with the lower correlation coefficients after 100th, the features of the absolute vorticity are more southward out of the Mei-yu area. Some modes show weaker vorticity features, or even some characteristics of a typhoon (Fig. 5k-o), which is obviously inconsistent with the referential weather system in the background. Those historical forecasting samples that are clearly different from the atmospheric conditions at the time of

assimilation should be discarded.

The results indicate that the historical forecasting samples possessing similar features with the background atmospheric circulation could be selected by calculating the correlation coefficients between the absolute vorticity of historical forecasting samples and background at the assimilation time. Therefore, more reasonable selected historical forecasting samples can be introduced into the hybrid data assimilation system.

4. Single observation tests

Single observation tests are carried out to investigate the structure of analysis increments of 3DVar and hybrid experiments base on different samples. According to the ranking order described above, single observation tests of selected historical forecasting samples, ensemble forecasting samples, and their combinations are listed as follows:

H50: top 50 selected historical forecasting samples according to the ranking list from high to low;
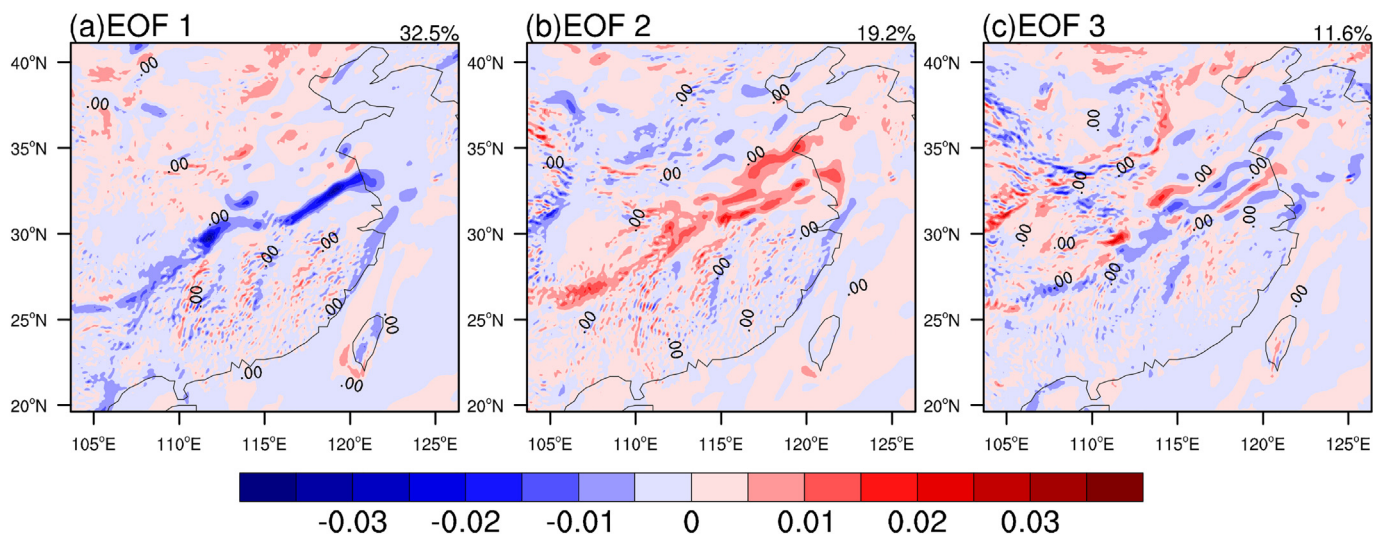
E50: 50 initial ensemble samples are constructed by adding

Fig. 3. Spatial patterns for the (a) first, (b) second and (c) third EOF mode of absolute vorticity in the background at 0600 UTC 1 July 2016.
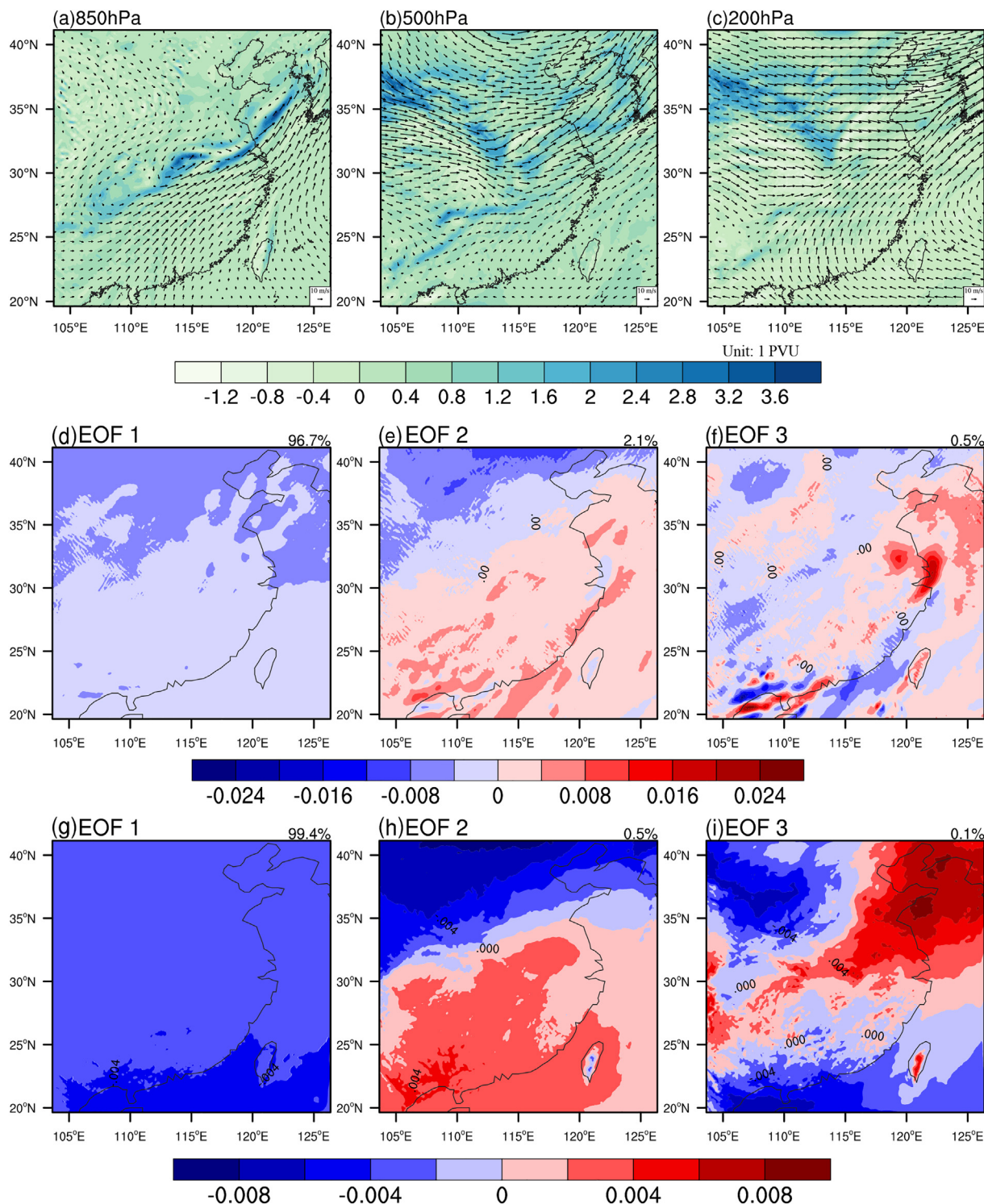
Fig. 4. The same as Figs. 2 and 3, but for the potential vorticity (a–f) and temperature (g–i) in the background at 0600 UTC 1 July 2016.

Gaussian random noise to analysis in the control variable space depending on static background error (known as "RandomCV" in WRFDA; Barker, 2005; Torn et al., 2006) and then updated by ETKF (ensemble transform Kalman filter technique to update the ensemble perturbations in WRFDA; Bishop et al., 2001; Wang and Bishop, 2003) scheme every 6 h in following two-day partial cycle referring to Chen et al. (2018);

E20: 20 ensemble forecasting samples picked up randomly from E50;

E20H30: 20 ensemble forecasting samples from E20 combined with the top 30 selected historical forecasting samples according to the ranking list from high to low.

The domain is configured with 41 vertical levels up to 50 hPa. A pseudo zonal wind (U) observation is placed at position (33°N, 116°E) on the 26th model level. The innovation (i.e. observation minus background) of U is 1.0 m s^{-1}; the observation error is 1.0 m s^{-1}; the horizontal localization length scale which determines the degree of ensemble covariance localization is 200 km; and the ensemble weighting coefficient factor is set to 0.75, which are the optimal
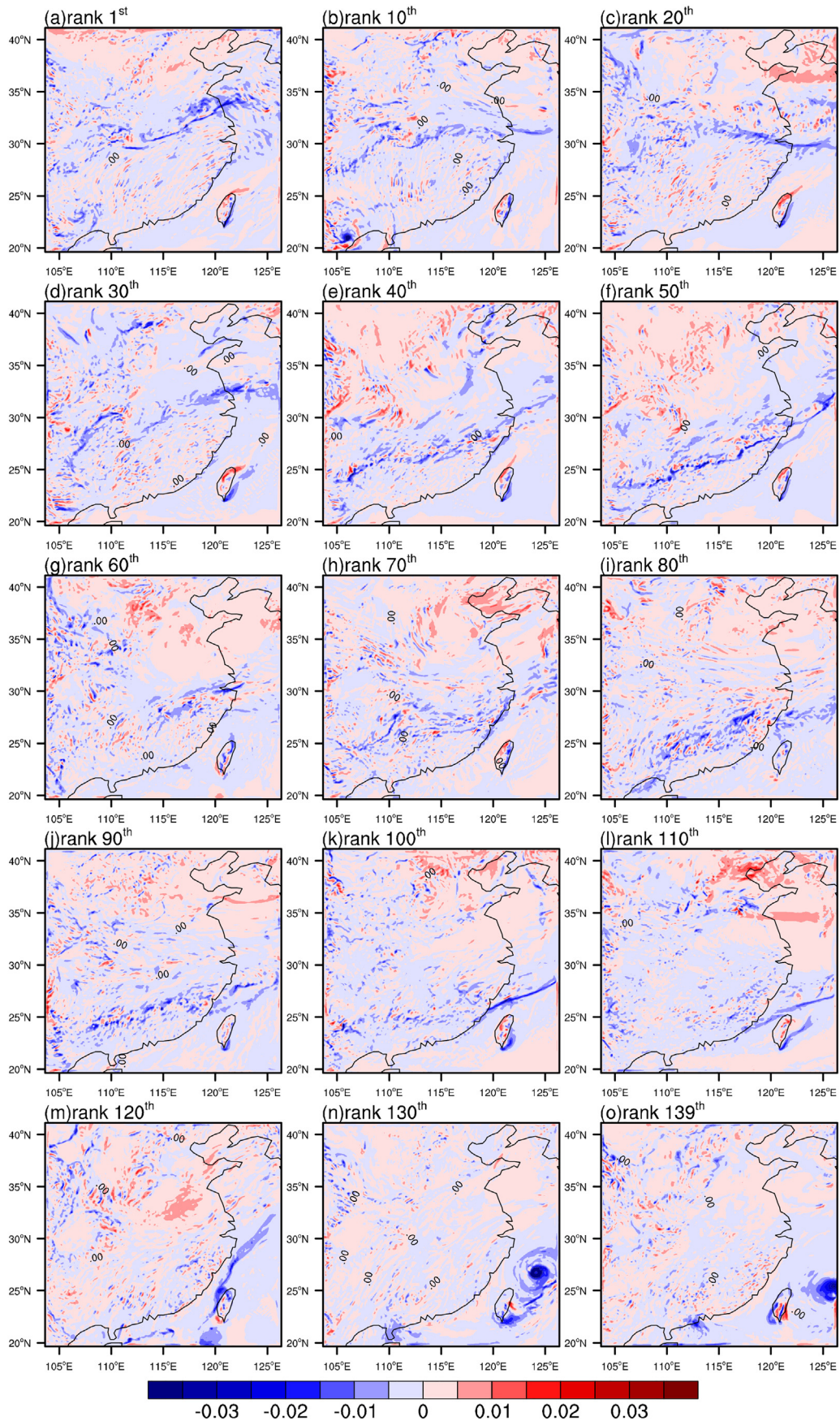
Fig. 5. The interval display for the first modes of the decomposed absolute vorticity fields of the 139 historical forecasting samples. The order is arranged according to the correlation coefficient from the highest (a) to lowest (o). The first modes ranking from 10 to 130 at ten intervals after sorting in descending order of correlation coefficient are shown in (b–n).
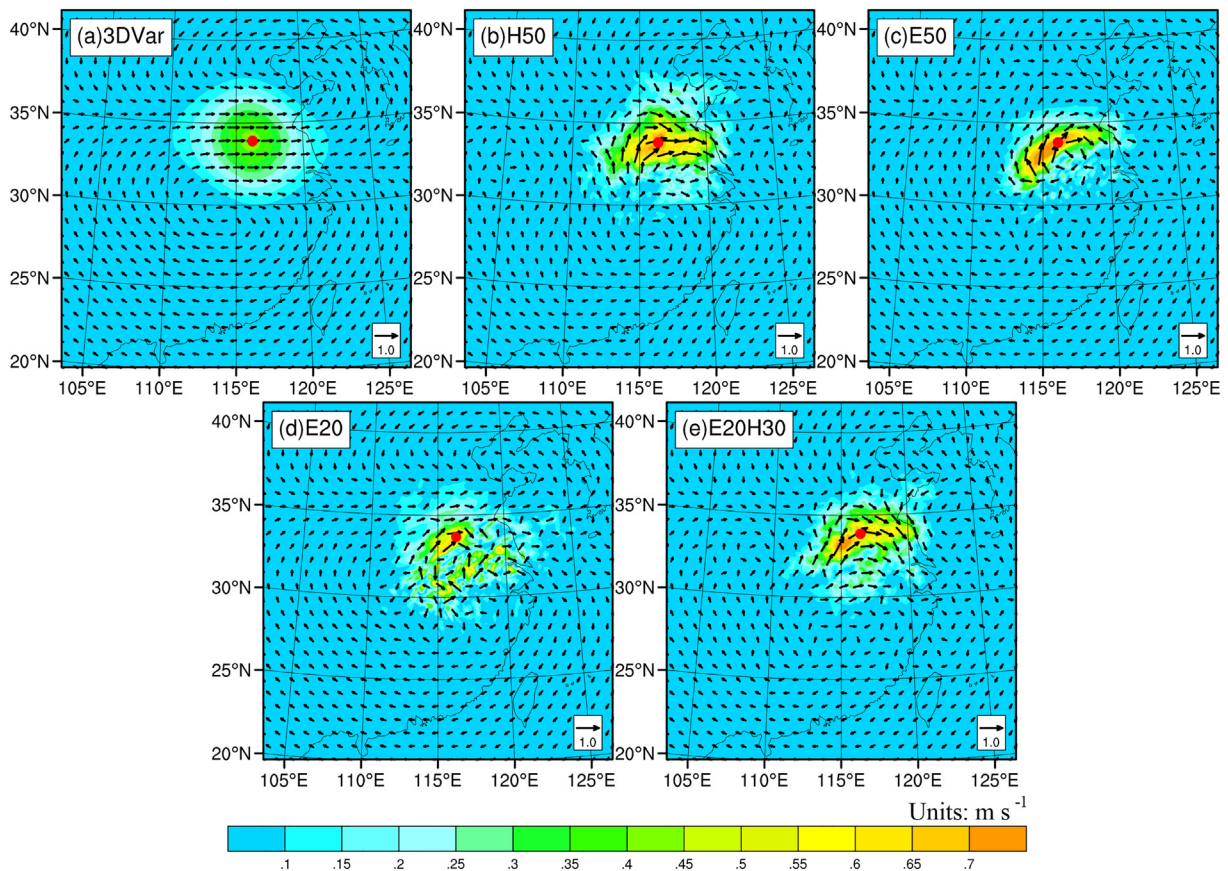
Fig. 6. Analysis increments of wind (vector, shaded; m s^{-1}) at the 26th (~200 hPa) level after assimilating the single **U** observation (red dot) with the weighting factor 0.75, (a) 3DVar, (b) H50, (c) E50, (d) E20 and (e) E20H30. (For interpretation of the references to colour in this figure legend, the reader is referred to the web version of this article.)

configurations referring to Chen et al. (2018). The background forecasts and ensembles in the single observation tests are taken from 0000 UTC 2 July 2016.

Analysis increments of wind after assimilating the single **U** observation are shown in Fig. 6. The wind analysis increments of 3DVar show the isotropic and homogeneous structure (Fig. 6a). Different from 3DVar, the wind increments of H50 (Fig. 6b) are anisotropic and inhomogeneous because of the historical forecast differences obtained via selected historical forecasting samples. The increments of H50 (Fig. 6b) show the similar flow-dependent feature with E50 (Fig. 6c) due to the selected historical forecasting samples based on the current atmospheric state, while Fig. 6b presents broader correlations than Fig. 6c. However, the increments of E20 (Fig. 6d) are different from those in E50, which fails to display the reasonable flow-dependent feature because of the limited samples. Fig. 6e shows that the increments of sample-combined experiment E20H30 present some of common features of E50 and H50, which means the flow-dependent information can also be derived from the combination of those two types of samples.

5. Cycling data assimilation and forecasting experiments

5.1. Model and experiments design

The study is based on the Advanced Research Weather Research and Forecasting Model (ARW-WRF, hereafter "WRF"; Skamarock and Klemp, 2008) on version 3.9.1. All experiments are conducted over a single domain (Fig. 7). The horizontal grid resolution is 9 km with 271 × 271 mesh grid points and the domain is configured with 41 vertical levels up to 50 hPa. The Global Forecast System (GFS) 0.25° × 0.25° analyses and forecasts are used for the initial and
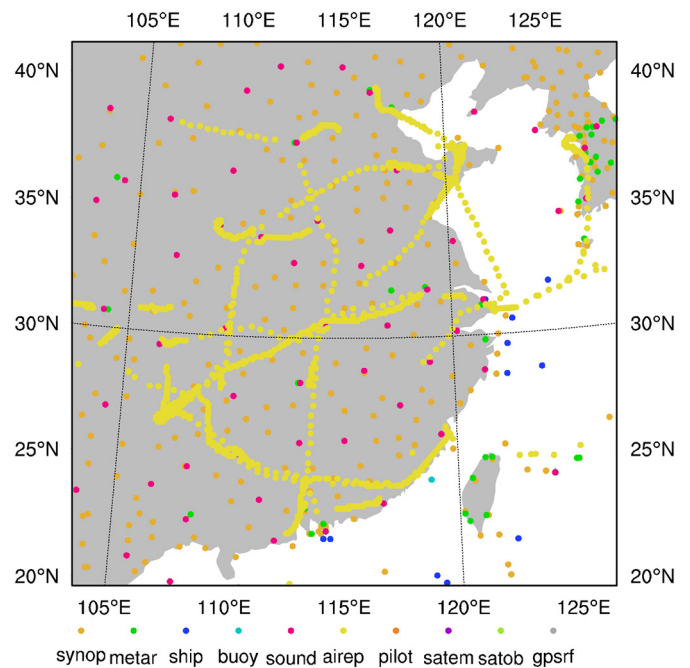

Fig. 7. The distributions of the observations assimilated at 0000 UTC 1 July 2016.

boundary conditions. The physical parameterizations are adopted as follows: the WRF Single-Moment 5-class microphysics scheme (WSM-5; Hong et al., 2004), the Yonsei University boundary layer scheme (YSU;

Hong et al., 2006), the Kaine-Fritsch cumulus parameterization scheme (Kain and Fritsch, 1990), the Dudhia shortwave radiation scheme (Dudhia, 1989) and the Rapid Radiative Transfer Model (RRTM) longwave radiation scheme (Mlawer et al., 1997).

The Global Telecommunication System (GTS) observations assimilated by WRFDA are also shown in Fig. 7. A variety of surface and upper-air meteorological observations are used from conventional observations and satellite products. The GTS observations pre-processing procedures such as data acquisition, decoding and quality control for all experiments are performed in the modules of WRFDA.

The static background error covariance for the variational system is estimated by the National Meteorological Center (NMC) method (Parrish and Derber, 1992). The NMC method is applied to calculate the difference between 24 h and 12 h forecasts valid at the same time (i.e., every 0000 and 1200 UTC) during the one-monthly period from 0000 UTC 1 July to 1800 UTC 31 July in 2015. The option 5 of control variables (known as "CV5" in WRFDA; Barker, 2005) are chosen to formulate the background error covariance in this study. With CV5, the control variables are in eigenvector space including stream function (ψ), unbalanced velocity potential (χ_u), unbalanced temperature (T_u), pseudo relative humidity ($RH_{s,u}$), and unbalanced surface pressure ($P_{s,u}$).

To compare and test the effects of different samples and their combinations in the WRFDA system, five groups of experiments are designed as follows: 3DVar, Hybrid-H50, Hybrid-E50, Hybrid-E20, Hybrid-E20H30. The experiment 3DVar is the control run using the three-dimension variational method, and others are all sample-based experiments in the hybrid data assimilation system.

The sample selection and combination configurations are consistent with the experimental settings in section 4. The experiments of Hybrid-H50, Hybrid-E50 and Hybrid-E20H30 are designed and compared to display the effects with the proportion change between the ensemble forecasting samples and the historical forecasting samples with 50 total samples. Hybrid-E20 and Hybrid-E20H30 are designed to show the impacts of extra 30 selected historical forecasting samples.

The ensemble samples in this study are initialized with the RandomCV method that works by adding random noise to the initial conditions (Barker, 2005; Torn et al., 2006) and updated by ETKF with the following cycle. The ensemble weighting factor is set to 0.75 and the covariance localization length scale is set to 200 km same as the configurations in Section 4. 19-day cycling data assimilation and forecasting experiments from 0000 UTC 19 June to 0000 UTC 7 July covering the Mei-yu period in 2016 are conducted. The assimilation frequency is 6 h, so totally 75 assimilation cases are tested.

5.2. Computational costs

Saving computation resources comes to one of the most important reasons for combining ensemble forecasting samples with historical forecasting samples. Table 1 lists the computing time consumption of 3DVar and other hybrid experiments with differential sample configuration. All of the experiments are carried out on large high-performance computing shared service platform supported by Nanjing University of Information Science and Technology (NUIST) with 56 processors. The CPU is Intel(R) Xeon(R) CPU E5–2680 v4, and running memory is 128G. The Operating system is Lenovo Flex System

enterprise server CentOS 7.3.

It can be seen that 3DVar takes 712 min for 19-day cycling, which is 4.67% of Hybrid-E50. The computing time consumption of Hybrid-H50 is comparable with 3DVar. It requires slightly extra 125 min due to the use of extended control variables in the analysis step. The computing time consumption of Hybrid-E20H30 is close to Hybrid-E20, both are around 43% of Hybrid-E50. It is clear that computational consumption for each experiment results mainly from ETKF-based ensemble forecasting processes. By combining the selected historical forecasting samples, the samples of Hybrid-E20H30 are extended on the premise of taking approximate computing resources of Hybrid-E20.

5.3. Results of cycling data assimilation and forecasts

5.3.1. Verification against GFS analysis

To evaluate the performance of five experiments during the rainfall period, the average root-mean-square errors (RMSEs) of horizontal winds (U, V), temperature (T), and specific humidity (Q) between the five experiments and the GFS analyses at 0.25° × 0.25° resolution are calculated. The GFS analysis as a reference has the advantages of using the 4DVar-based EnKF-variational hybrid data assimilation system and assimilating multiple observations (Kleist and Ide, 2015; Zhou et al., 2016). And the RMSEs are calculated against GFS analyses for verifying large-scale information of the model forecasts.

Fig. 8 displays the vertical profiles of mean RMSEs between the analyses of the five experiments and GFS over 19 days from 0600 UTC 19 June to 0000 UTC 7 July 2016. The experiment 3DVar appears to yield the largest RMSEs, while the experiment Hybrid-E50 shows the best performance. Compared with 3DVar, the improvements of Hybrid-H50 are slightly limited partly because of some of the low-ranking historical forecasting samples in Hybrid-H50 are not able to estimate the background error covariance well during the whole process of cycling assimilation and forecasting. The RMSEs performance of Hybrid-E20H30 is clearly greater to Hybrid-E20 for the variables (i.e. U, V, T, Q), although both of them are better than Hybrid-H50. Furthermore, the experiment Hybrid-E20H30 performs close to the best performing Hybrid-E50. It should be noted that the experiment Hybrid-E20H30 consumes less than half of the computational resources of experiment Hybrid-E50, slightly more than Hybrid-E20 (Table 1). The results indicate the positive impact of combining the 30 selected historical forecasting samples, which is because flow-dependent background error covariance features are introduced in the assimilation.

Fig. 9 displays the vertical profiles of mean RMSEs of 6 h and 24 h experimental forecasts and related GFS forecasts against the GFS analyses over the same area. It should be noted that the continuous cycling assimilation and forecasting experiments are carried out with 6 h spin-up and two-day partial cycles mentioned above. Therefore, the averaged RMSEs of equivalent 6 h GFS forecasts are actually calculated from the T + 12, T + 18, ..., T + 54 GFS forecasts at the initial time (T) of each cycling experiments. Similarly, the RMSEs of 24 h GFS forecasts are calculated from the T + 30, T + 36, ..., T + 72 GFS forecasts. It shows that the equivalent GFS forecasts perform obviously larger RMSEs in general (purple line), due to the GFS forecasts forecasting without assimilating observations. Compared with it, the cycling assimilation and forecasting experiments have benefits from the available observations and lead to improved estimation of the atmospheric state

Table 1
The sample configuration and computational cost of the assimilation experiments.

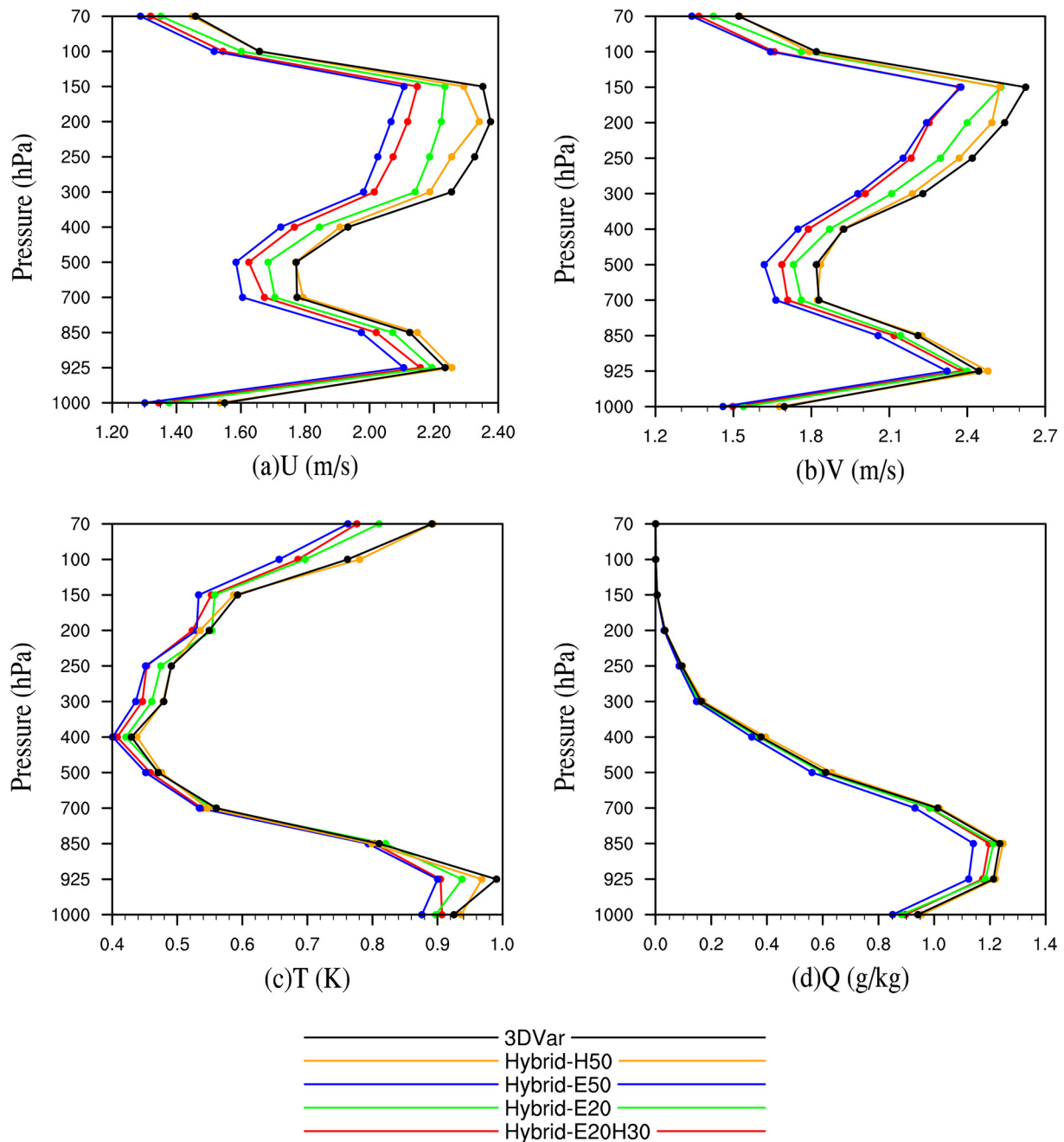| Experiments	3DVar	Hybrid-H50	Hybrid-E50	Hybrid-E20	Hybrid-E20H30
Ensemble forecasting samples	/	0	50	20	20
Selected historical forecasting samples	/	50	0	0	30
Cost (min)	712	837	15,256	6614	6671
Percent (%)	4.67	5.49	100.00	43.35	43.73

Fig. 8. Vertical profiles of the analyses RMSEs of (a) U (m s^{-1}), (b) V (m s^{-1}), (c) T (K) and (d) Q (g/kg) against the GFS analyses from 0600 UTC 19 June to 0000 UTC 7 July in 2016.

(Barker et al., 2004). As the forecast errors accumulate along the leading time, it can be seen that the experimental RMSEs become larger, and the differences of errors between the experiments are small by T + 24 (Fig. 9). The reason is that the boundary conditions are the same for these experiments and the influences of initial conditions are reduced. The improvements of all hybrid experiments also decrease in four fields (i.e. U, V, T, Q) from 6 h to 24 h forecasts. The performance of Hybrid-E20H30 is still close to that of Hybrid-E50 and better than other experiments especially in variables of U/V (Fig. 9a-b). These improvements from the Hybrid-E20H30 are likely to be associated with the effects of selected historical forecasting samples.

The results of RMSEs indicate that the Hybrid-E20H30 based on the combination of ensemble forecasting samples and selected historical forecasting samples performs better than the experiment 3DVar and Hybrid-E20 overall. The improvements can be seen through four basic

variables (i.e. U, V, T, Q) in both analyses (Fig. 8) and forecasts (Fig. 9), especially through U/V variables (Fig. 8a-b, Fig. 9a-b). And the experiment Hybrid-E20H30 has the advantage of using computing resources more efficiently than other ETKF-based hybrid experiments, which is mentioned above in Section 5.2 (Table. 1).

5.3.2. Precipitation forecast skill

To quantify the performance of precipitation of all five different experiments, Fractions Skill Score (FSS, Roberts and Lean, 2008) and Equitable Threat Score (ETS; Clark et al., 2010) are used to evaluate the precipitation forecast skill. FSS varies from 0 to 1, with 0 representing no overlap between observation and prediction field, and 1 representing complete overlap (Roberts and Lean, 2008). The ETS ranges from −1/3 to 1, where −1/3 is the lower limit. For ETS, 0 indicates no skill and 1 indicates a perfect skill (Clark et al., 2010). The observed
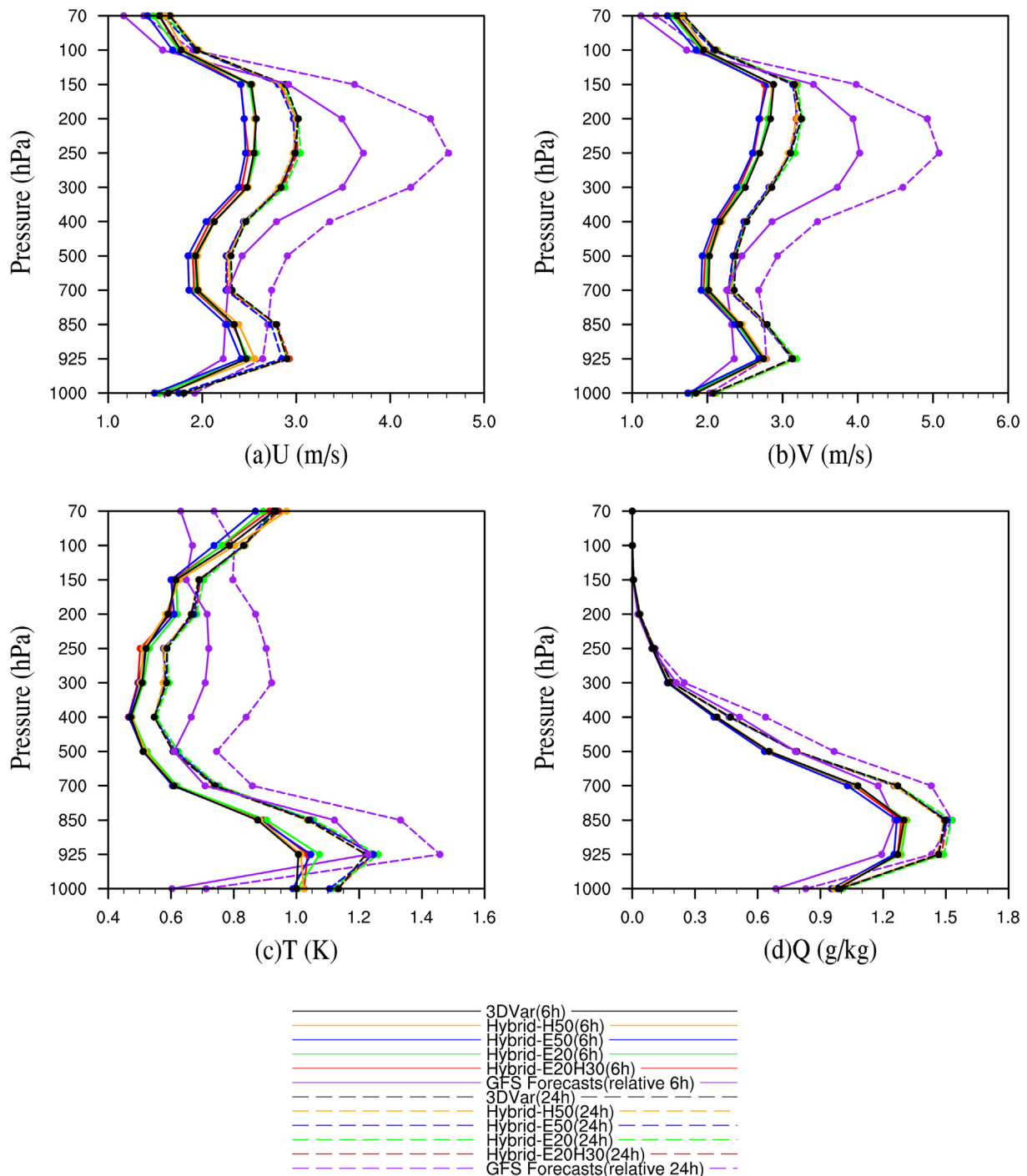
Fig. 9. The same as Fig. 8, but the 6 h forecast (solid line) and 24 h forecast (dotted line) RMSEs of (a) U (m s^{-1}), (b) V (m s^{-1}), (c) T (K) and (d) Q (g/kg) against the GFS analyses.

precipitation products are the China Hourly Merged Precipitation Analysis (CHMPA) with 0.1° latitude × 0.1° longitude spatial resolution (Shen et al., 2014). The scoring area covering the rainfall procession is set to (114°E-121°E, 28°N-32°N), and the horizontal scale of FSSs is 18 km in this study.

The time series of FSSs and ETSs with the threshold of 1 mm h^{-1} averaged from 75 forecasts are presented in Fig. 10. It can be seen that all the hybrid experiments are clearly superior to 3DVar experiment , and the Hybrid-E50 experiment performed best in general. Although better than 3DVar experiment, the Hybrid-H50 experiment is still scored lower than those hybrid experiments using ensemble forecasting

samples. In the first 6 h, the FSS and ETS of Hybrid-E20H30 are close to Hybrid-E50 and it is superior to Hybrid-E20 in most forecasts. Note that both experiments of Hybrid-E20H30 and Hybrid-E20 use the same ensemble forecasting samples and require roughly equal computational costs, but the sample size of the Hybrid-E20H30 is larger. The increase of the precipitation forecast skill in the Hybrid-E20H30 experiment could be attributed to the utility of 30 selected historical forecasting samples, which provide more available samples and alleviate the defects due to the limited sample size.
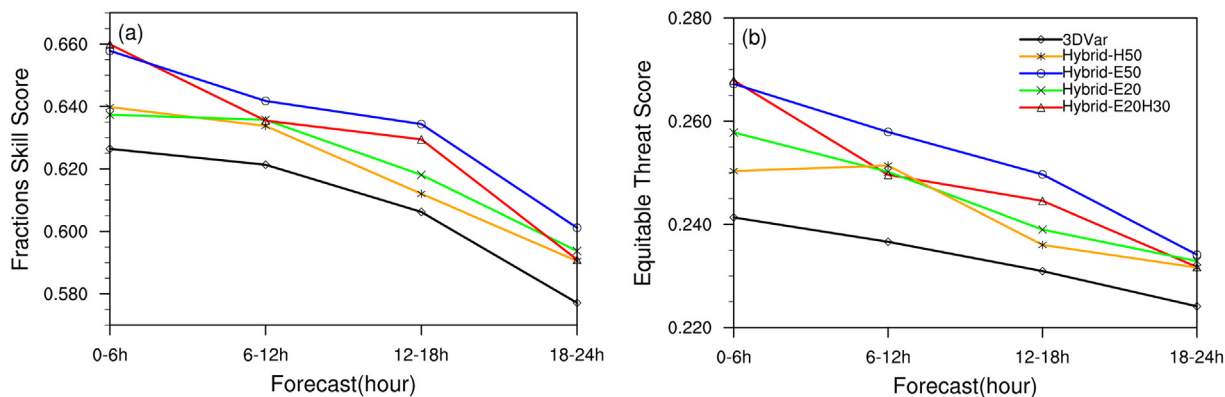
Fig. 10. (a) Fractions skill scores with 18-km radius and (b) Equitable threat scores for the 6 h accumulated precipitation threshold of 1 mm h^{-1} along the forecast time from 0600 UTC 19 June to 0000 UTC 7 July in 2016. The precipitation observation used in the score are from the China Hourly Merged Precipitation Analysis (CHMPA) with 0.1° latitude × 0.1° longitude spatial resolution.

6. Diagnostics for a heavy rainfall event

6.1. Accumulated precipitation

In early July, there was a continuous heavy rainfall event over Yangtze-Huai River Basin. The 24 h accumulated precipitation initialized at 0000 UTC 2 July 2017 is presented in Fig. 11. It can be seen that the observed 24 h accumulated precipitation derived from CHMPA roughly extends along the Southwest-Northeast direction, with the maximum value exceeding 120 mm (Fig. 11a). The 3DVar experiment obviously underestimates the maximum value (Fig. 11b), while the precipitation intensity is enhanced in all the hybrid experiments (Fig. 11c-f). However, it shows that the precipitation of Hybrid-H50 produces a discontinuous rain-belt distribution (Fig. 11c). The Hybrid-E20 overestimates the precipitation at east coast area and has some deviations from the observation position (Fig. 11e). Compared with other methods, Hybrid-E20H30 and Hybrid-E50 show better prediction in terms of precipitation location and intensity (Fig. 11d, Fig. 11f). Furthermore, Hybrid-E20H30 occupies less than half of the computing resources of Hybrid-E50.
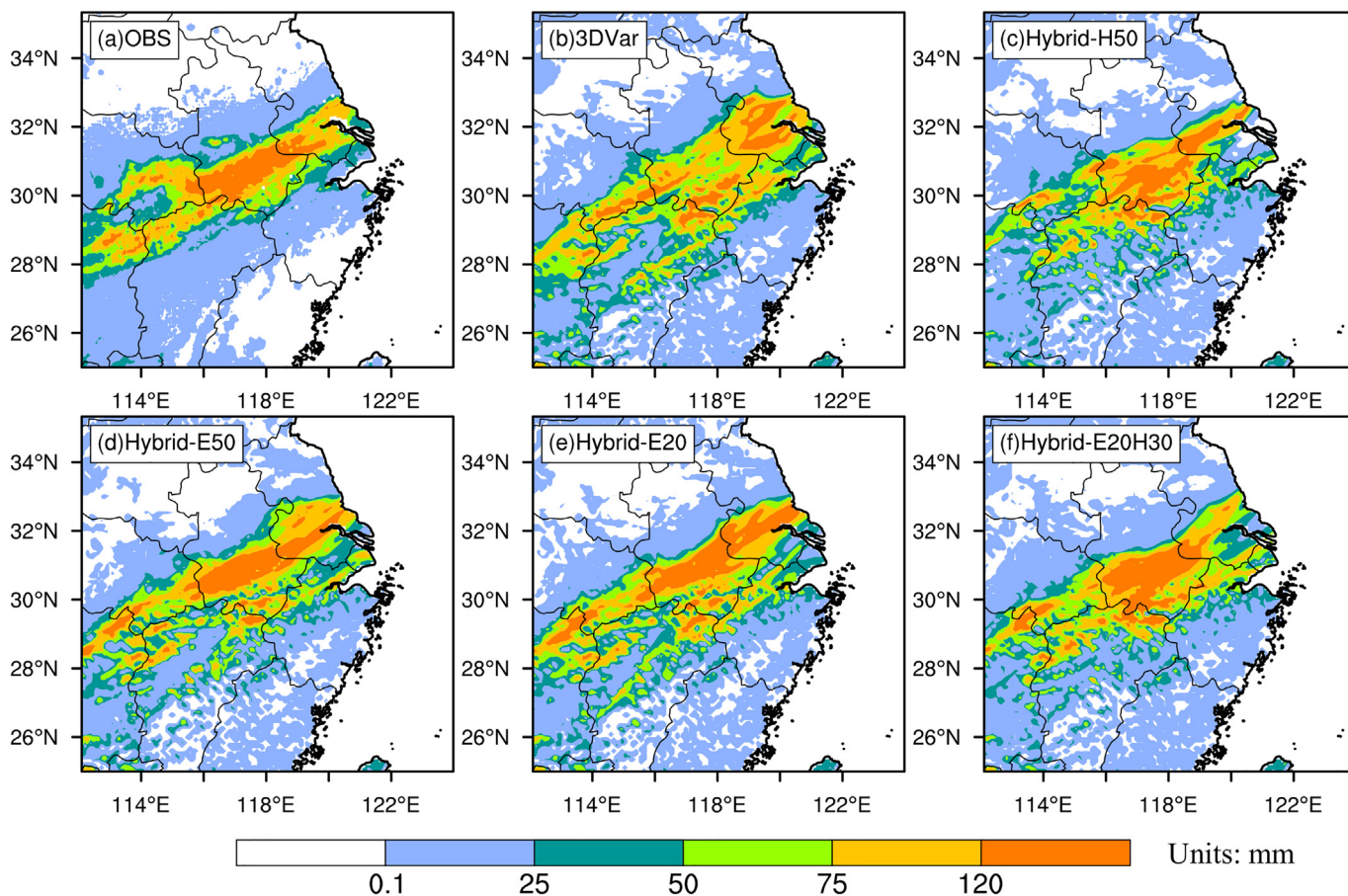

Fig. 11. The distribution of 24 h accumulated precipitation beginning at 0000 UTC 2 July 2016 for (a) the precipitation observation, (b) 3DVar, (c) Hybrid-H50, (d) Hybrid-E50, (e) Hybrid-E20 and (f) Hybrid-E20H30.
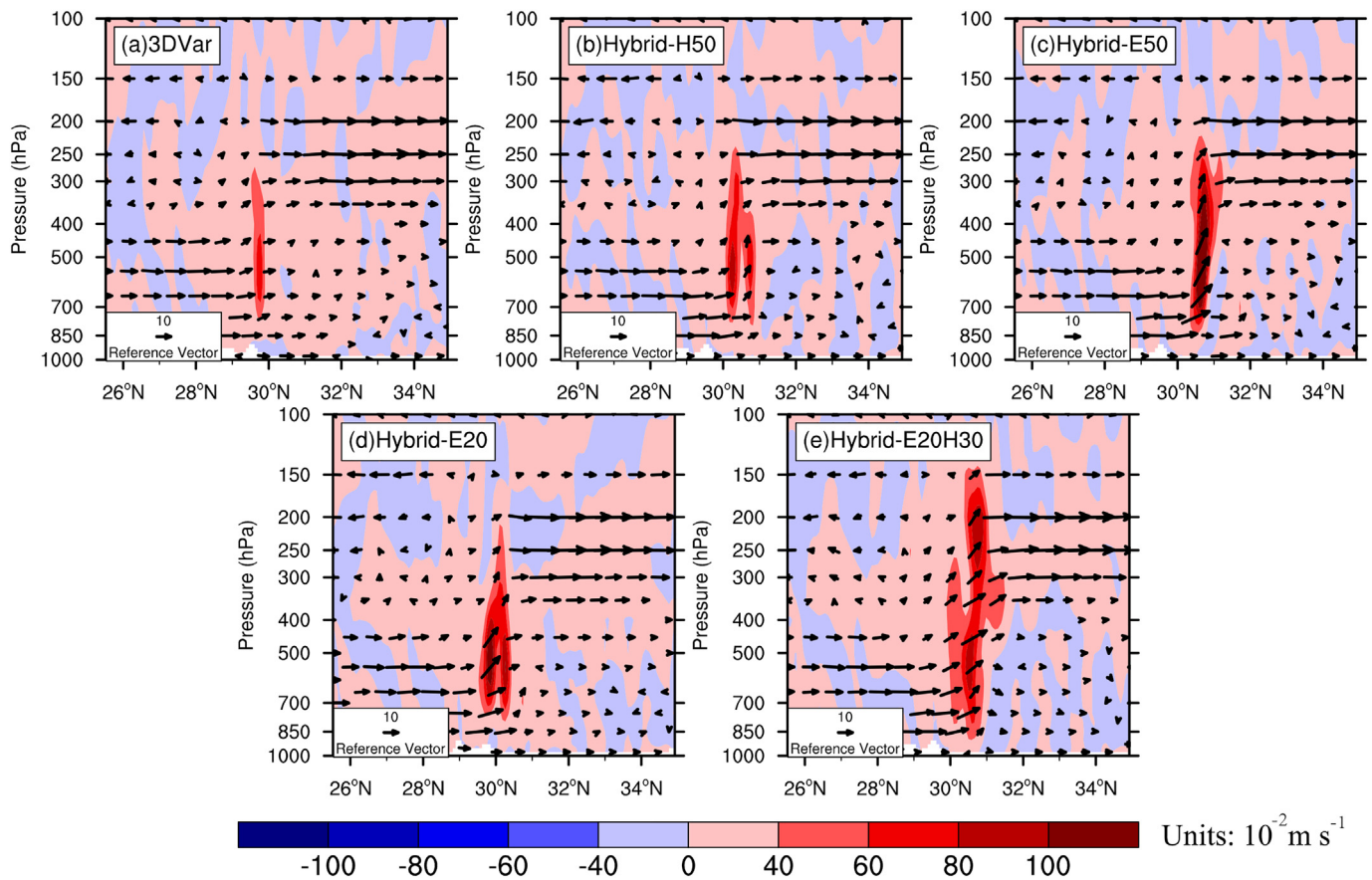
Fig. 12. Cross sections of vertical velocity of 18 h forecast (shaded; 10^{-2} m s^{-1}) along the rainfall center of 117.5°E at 0018 UTC 2 June 2016. (a) 3DVar, (b) Hybrid-H50, (c) Hybrid-E50, (d) Hybrid-E20, and (e) Hybrid-E20H30.

6.2. Vertical velocity and water vapor

The vertical cross sections of the vertical velocity of 18 h forecasts along 117.5°E in the center of heavy precipitation at 0018 UTC 02 July are presented in Fig. 12. It shows that there is no strong vertical uplift flow support at the heavy rainfall area in the 3DVar experiment (Fig. 12a). Compared to the 3DVar, the vertical velocity of Hybrid-H50 (Fig. 12b) is intensified, but it is still relatively weaker than Hybrid-E50 (Fig. 12c). The experiment of Hybrid-E20H30 is capable of simulating deepest vertical lift movements concentrated at 30°N (Fig. 12e), which contributes to the improvement of precipitation simulation.

The vertical cross sections of the relative humidity of 18 h forecasts along 117.5°E valid at 0018 UTC 02 July are presented in Fig. 13 to indicate the convergence of moisture. The strong rainfall mainly appears near 29°N ~ 31°N. The 3DVar experiment yields weaker relative humidity in the precipitation area between 500 hPa and 700 hPa (Fig. 13a). Insufficient conditions of water vapor and weak uplift flow result in the deviation of precipitation forecast in this region. The sample-based hybrid methods strengthen the moisture condition (Fig. 13b-e). It can be seen that the relative humidity of Hybrid-E20 (Fig. 13d) is still inadequate compared with Hybrid-E50 (Fig. 13c). The experiment of Hybrid-E20H30 is capable of simulating stronger widespread relative humidity bands with good continuity (Fig. 13e), which favors the water vapor conditions for the rainfall process.

7. Summary

To reduce the computational burden of ensemble forecast and introduce the inhomogeneous and flow-dependent background error covariance to hybrid data assimilation system, the historical forecasting samples selected by the EOF method are utilized to combine with the ensemble forecasting samples. The impact of selected historical forecasting samples is assessed by single observation tests and 19-day continuous cycling data assimilation and forecasting experiments of the Mei-yu period in 2016.

The selection process shows that the selected historical forecasting samples with high rankings show similar dynamical feature to the background, while those samples with low rankings are obviously different from the weather situation at the time of assimilation. Thus the historical forecasting samples which are closer to the atmospheric situation can be selected effectively from all historical samples for hybrid assimilation experiments by EOF method.

Single observation tests show the wind increments of the experiment with 20 ensemble forecasting samples fails to display the reasonable flow-dependent feature due to limited samples. The anisotropic and inhomogeneous wind increments are obtained by using 50 selected historical forecasting samples, which are similar to the increments of the experiment with 50 ensemble forecasting samples. Wind increments of the sample-combined experiment has some of common features of experiments with 50 ensemble forecasting samples and 50 selected historical forecasting samples.

Compared with the experiment of 20 ensemble forecasting samples, the wind increments of experiment with combining samples are more similar to those with 50 ensemble forecasting samples. The results of single observation tests show that the use of selected historical forecasting samples is able to provide reasonable flow-dependent background error covariance for the data assimilation system.

Results from the cycling experiments show that analyses and forecasts skills in the hybrid experiments with the selected historical forecasting samples are improved compared to 3DVar in terms of the RMSEs as well as the precipitation forecasts. Although using only historical forecasting samples in hybrid experiment performs slightly
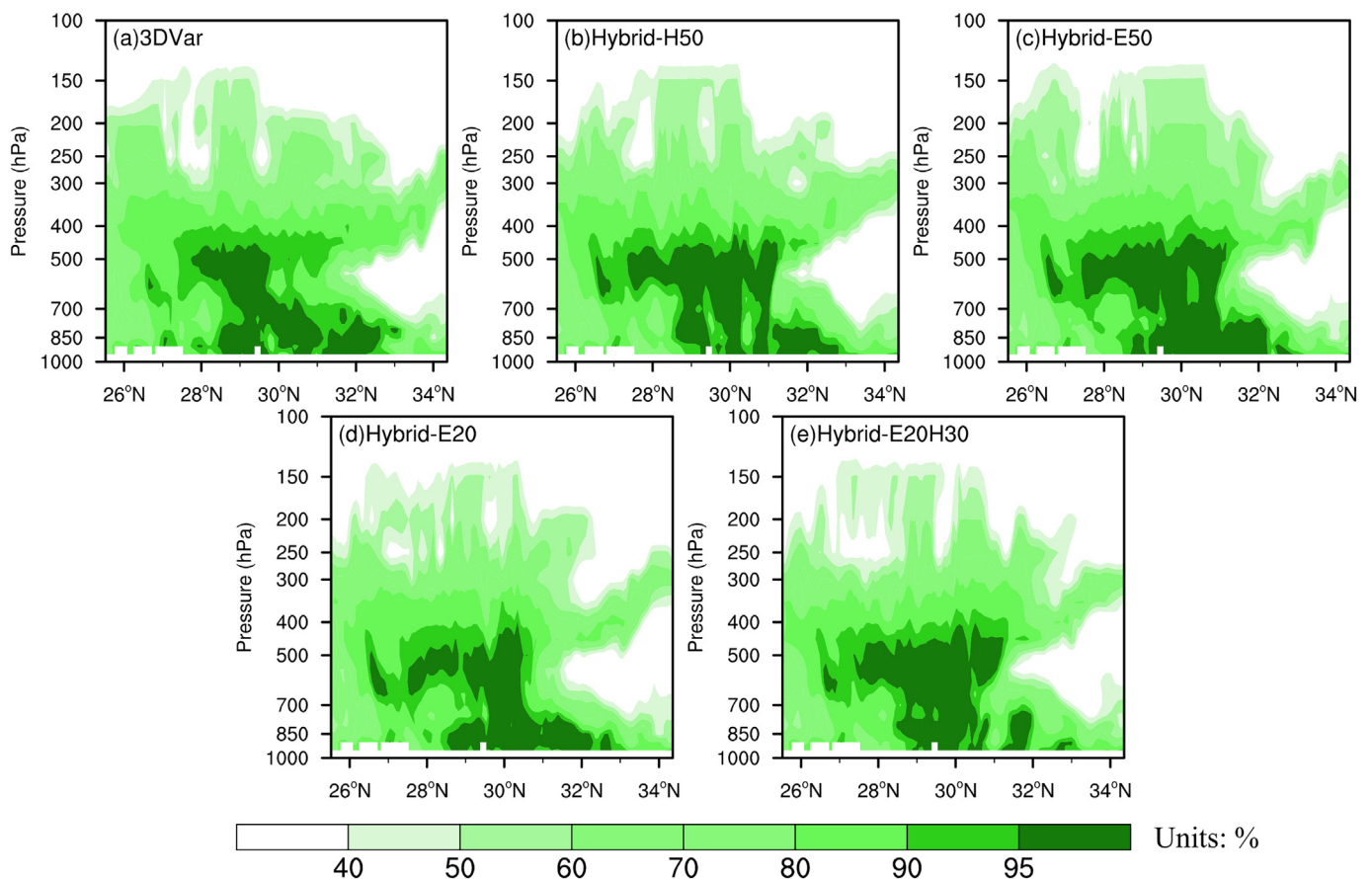
Fig. 13. Cross sections of relative humidity of 18 h forecast (shaded; %) along the rainfall center of 117.5°E at 0018 UTC 2 June 2016. (a) 3DVar, (b) Hybrid-H50, (c) Hybrid-E50, (d) Hybrid-E20, and (e) Hybrid-E20H30.

better than 3DVar at the analysis time and gives inferior results of forecasts, the advantages of historical samples are demonstrated clearly through the results of sample-combined hybrid experiment. The performance is improved by introducing the selected historical samples on the premise of the same ensemble forecasting samples and close to the ensemble forecasting samples experiment with the full sample size. These results could be attributed to the optimal selected historical forecasting samples by the EOF method, because the selected historical forecasting samples are efficiently utilized to enrich the available ensembles and introduced to provide flow-dependent background error covariance.

Besides, the computational efficiency analysis further explains the advantage of cost-saving of computation using selected historical forecasting samples. The computing resources spent on the sample-combined hybrid experiment are roughly equal to the hybrid experiment with 20 ensemble forecasting samples, much less than the experiment with 50 ensemble forecasting samples. Such cost-saving is necessary for departments with tight computing resources.

It should be noted that there are only 139 alternative historical forecasting samples used in the study. The performance of historical-sample-based hybrid experiments could be further improved when better samples are selected from the storage of more historical forecasting samples. Furthermore, the absolute vorticity is regarded as the only selection index in this study. More synthetical indicator could be considered for more rational selection.

Declaration of Competing Interest

The authors declare that they have no known competing financial interests or personal relationships that could have appeared to

influence the work reported in this paper.

References

Kleist, Ide, K., 2015. An OSSE-based evaluation of hybrid variational-ensemble data assimilation for the NCEP GFS. Part I: system description and 3D-hybrid results. Mon. Weather Rev. 143, 433–451. https://doi.org/10.1175/MWR-D-13-00351.1.

Bannister, R.N., 2017. A review of operational methods of variational and ensemble-variational data assimilation: ensemble-variational data assimilation. Q. J. R. Meteorol. Soc. 143, 607–633. https://doi.org/10.1002/qj.2982.

Barker, D.M., 2005. Southern high-latitude ensemble data assimilation in the Antarctic Mesoscale Prediction System. Mon. Weather Rev. 133, 3431–3449. https://doi.org/10.1175/MWR3042.1.

Barker, D.M., Huang, W., Guo, Y.R., et al., 2004. A three-dimensional variational data assimilation system for MM5: implementation and initial results. Mon. Weather Rev. 132, 897–914. https://doi.org/10.1175/1520-0493(2004)132<0897:atvdas>2.0.co;2.

Bishop, B., Etherton, J., Majumdar, S.J., 2001. Adaptive sampling with the ensemble transform Kalman filter. Part I: Theoretical aspects. Mon. Weather Rev. 129, 420–436. https://doi.org/10.1175/1520-0493(2001)129<0420:ASWTET>2.0.CO;2.

Chen, George Tai-Jen, 2004. Research on the phenomena of Meiyu during the past quarter century: an overview. East Asian Monsoon 357–403. https://doi.org/10.1142/9789812701411_0010.

Chen, Y., Wang, J., Gao, Y., Chen, X., Wang, H., Huang, X.-Y., 2018. Refinement of the use of inhomogeneous background error covariance estimated from historical forecast error samples and its impact on short-term regional numerical weather prediction. J. Meteorol. Soc. Jpn Ser II 96, 429–446. https://doi.org/10.2151/jmsj.2018-048.

Clark, A.J., Gallus, W.A., Weisman, M.L., 2010. Neighborhood-based verification of precipitation forecasts from convection-allowing NCAR WRF model simulations and

the operational NAM. Weather Forecast. 25, 1495–1509. https://doi.org/10.1175/2010WAF2222404.1.

Dimet, F.-X.L., Talagrand, O., 1986. Variational algorithms for analysis and assimilation of meteorological observations: theoretical aspects. Tellus A 38A, 97–110. https://doi.org/10.1111/j.1600-0870.1986.tb00459.x.

Dudhia, J., 1989. Numerical study of convection observed during the winter monsoon experiment using a mesoscale two-dimensional model. J. Atmos. Sci. 46, 3077–3107. https://doi.org/10.1175/1520-0469(1989)046<3077:NSOCOD>2.0.CO;2.

Evensen, G., 1994. Sequential data assimilation with a nonlinear quasi-geostrophic model using Monte Carlo methods to forecast error statistics. J. Geophys. Res. Oceans 99, 10143–10162. https://doi.org/10.1029/94JC00572.

Evensen, G., 2003. The Ensemble Kalman Filter: theoretical formulation and practical implementation. Ocean Dyn. 53, 343–367. https://doi.org/10.1007/s10236-003-0036-9.

Gao, S., Zhou, Y., Lei, T., 2002. Structural features of the Meiyu front system. J. Meteorol. Res. 195–204.

Hamill, T.M., Snyder, C., 2000. A hybrid ensemble kalman filter-3d variational analysis scheme. Mon. Weather Rev. 128, 2905–2919. https://doi.org/10.1175/1520-0493(2000)128<2905:AHEKFV>2.0.CO;2.

Hong, S.-Y., Dudhia, J., Chen, S.-H., 2004. A revised approach to ice microphysical processes for the bulk parameterization of clouds and precipitation. Mon. Weather Rev. 132, 103–120. https://doi.org/10.1175/1520-0493(2004)132<0103:ARATIM>2.0.CO;2.

Hong, S.-Y., Noh, Y., Dudhia, J., 2006. A new vertical diffusion package with an explicit treatment of entrainment processes. Mon. Weather Rev. 134, 2318–2341. https://doi.org/10.1175/MWR3199.1.

Huang, X.-Y., Xiao, Q., Barker, D.M., Zhang, Xin, Michalakes, J., Huang, W., Henderson, T., Bray, J., Chen, Y., Ma, Z., Dudhia, J., Guo, Y., Zhang, Xiaoyan, Won, D.-J., Lin, H.-C., Kuo, Y.-H., 2009. Four-dimensional variational data assimilation for WRF: formulation and preliminary results. Mon. Weather Rev. 137, 299–314. https://doi.org/10.1175/2008MWR2577.1.

Kain, J.S., Fritsch, J.M., 1990. A one-dimensional entraining/detraining plume model and its application in convective parameterization. J. Atmos. Sci. 47, 2784–2802. https://doi.org/10.1175/1520-0469(1990)047<2784:AODEPM>2.0.CO;2.

Lorenc, A.C., 1986. Analysis methods for numerical weather prediction. Q. J. R. Meteorol. Soc. 112, 1177–1194. https://doi.org/10.1002/qj.49711247414.

Lorenc, A.C., 2003. The potential of the ensemble Kalman filter for NWP—a comparison with 4D-Var. Q. J. R. Meteorol. Soc. 129, 3183–3203. https://doi.org/10.1256/qj.02.132.

Lorenc, A.C., Bowler, N.E., Clayton, A.M., Pring, S.R., Fairbairn, D., 2015. Comparison of hybrid-4DEnVar and hybrid-4DVar data assimilation methods for global NWP. Mon. Weather Rev. 143, 212–229. https://doi.org/10.1175/MWR-D-14-00195.1.

Mlawer, E.J., Taubman, S.J., Brown, P.D., Iacono, M.J., Clough, S.A., 1997. Radiative transfer for inhomogeneous atmospheres: RRTM, a validated correlated-k model for the longwave. J. Geophys. Res. Atmos. 102, 16663–16682. https://doi.org/10.1029/97JD00237.

Monahan, A.H., Fyfe, J.C., Ambaum, M.H., Stephenson, D.B., North, G.R., 2009. Empirical orthogonal functions: the medium is the message. J. Clim. 22, 6501–6514. https://doi.org/10.1175/2009JCLI3062.1.

Parrish, D.F., Derber, J.C., 1992. The National Meteorological Center's spectral statistical-interpolation analysis system. Mon. Weather Rev. 120, 1747–1763. https://doi.org/10.1175/1520-0493(1992)120<1747:TNMCSS>2.0.CO;2.

Prezerakos, N.G., Flocas, H.A., Michaelides, S.C., 1997. Absolute vorticity advection and potential vorticity of the free troposphere as synthetic tools for the diagnosis and forecasting of cyclogenesis. Atmosphere-Ocean 35, 65–91. https://doi.org/10.1080/07055900.1997.9649585.

Ran, L., Li, N., Gao, S., 2013. PV-based diagnostic quantities of heavy precipitation: Solenoidal vorticity and potential solenoidal vorticity. J. Geophys. Res. Atmos. 118,

10506. https://doi.org/10.1002/jgrd.50294.

Roberts, N.M., Lean, H.W., 2008. Scale-selective verification of rainfall accumulations from high-resolution forecasts of convective events. Mon. Weather Rev. 136, 78–97. https://doi.org/10.1175/2007MWR2123.1.

Sampe, T., Xie, S.-P., 2010. Large-scale dynamics of the meiyu-baiu rainband: environmental forcing by the westerly Jet*. J. Clim. 23, 113–134. https://doi.org/10.1175/2009JCLI3128.1.

Schwartz, C.S., Liu, Z., 2014. Convection-permitting forecasts initialized with continuously cycling limited-area 3DVAR, ensemble Kalman filter, and "hybrid" variational-ensemble data assimilation systems. Mon. Weather Rev. 142, 716–738. https://doi.org/10.1175/MWR-D-13-00100.1.

Shen, Y., Zhao, P., Pan, Y., Yu, J., 2014. A high spatiotemporal gauge-satellite merged precipitation analysis over China. J. Geophys. Res.-Atmos. 119, 3063–3075. https://doi.org/10.1002/2013JD020686.

Skamarock, W.C., Klemp, J.B., 2008. A time-split nonhydrostatic atmospheric model for weather research and forecasting applications. J. Comput. Phys. 227, 3465–3485. https://doi.org/10.1016/j.jcp.2007.01.037.

Torn, R.D., Hakim, G.J., Snyder, C., 2006. Boundary conditions for limited-area ensemble Kalman filters. Mon. Weather Rev. 134, 2490–2502. https://doi.org/10.1175/MWR3187.1.

Van Den Dool, H.M., 1989. A new look at weather forecasting through analogues. Mon. Weather Rev. 117, 2230–2247. https://doi.org/10.1175/1520-0493(1989)117<2230:ANLAWF>2.0.CO;2.

Van Den Dool, H.M., 1990. Mirror images of atmospheric flow. Mon. Weather Rev. 119, 2095–2106. https://doi.org/10.1175/1520-0493(1991)119<2095:MIOAF>2.0.CO;2.

Wallace, J.M., Gutzler, D.S., 1981. Teleconnections in the geopotential height field during the Northern Hemisphere winter. Mon. Weather Rev. 109, 784–812. https://doi.org/10.1175/1520-0469(1981)109<0784:TITGHF>2.0.CO;2.

Wang, X., Bishop, C.H., 2003. A comparison of breeding and ensemble transform Kalman filter ensemble forecast schemes. J. Atmos. Sci. 60, 1140–1158. https://doi.org/10.1175/1520-0469(2003)060<1140:ACOBAE>2.0.CO;2.

Wang, X., Barker, D.M., Snyder, C., Hamill, T.M., 2008a. A hybrid ETKF-3DVAR data assimilation scheme for the WRF model. Part I: observing system simulation experiment. Mon. Weather Rev. 136, 5116–5131. https://doi.org/10.1175/2008MWR2444.1.

Wang, X., Barker, D.M., Snyder, C., Hamill, T.M., 2008b. A hybrid ETKF-3DVAR data assimilation scheme for the WRF model. Part II: real observation experiments. Mon. Weather Rev. 136, 5132–5147. https://doi.org/10.1175/2008MWR2445.1.

Wang, Y., Min, J., Chen, Y., Huang, X.-Y., Zeng, M., Li, X., 2017. Improving precipitation forecast with hybrid 3DVar and time-lagged ensembles in a heavy rainfall event. Atmos. Res. 183, 1–16. https://doi.org/10.1016/j.atmosres.2016.07.026.

Xue, M., Wang, D., Gao, J., Brewster, K., Droegemeier, K.K., 2003. The Advanced Regional Prediction System (ARPS), storm-scale numerical weather prediction and data assimilation. Meteorog. Atmos. Phys. 82, 139–170. https://doi.org/10.1007/s00703-001-0595-6.

Yuan, Y., Gao, H., Li, W., Liu, Y., Chen, L., Zhou, B., Ding, Y., 2017. The 2016 summer floods in China and associated physical mechanisms: a comparison with 1998. J. Meteorol. Res. 31, 261–277. https://doi.org/10.1007/s13351-017-6192-5.

Zhang, F., Zhang, M., Poterjoy, J., 2013. E3DVar: coupling an ensemble Kalman filter with three-dimensional variational data assimilation in a limited-area weather prediction model and comparison to E4DVar. Mon. Weather Rev. 141, 900–917. https://doi.org/10.1175/MWR-D-12-00075.1.

Zhou, X., Zhu, Y., Hou, D., Kleist, D., 2016. A comparison of perturbations from an ensemble transform and an ensemble Kalman filter for the NCEP global ensemble forecast system. Weather Forecast. 31, 2057–2074. https://doi.org/10.1175/WAF-D-16-0109.1.